

Reconstructing absorption and scattering distributions in quantitative photoacoustic tomography

T Tarvainen^{1,2}, B T Cox³, J P Kaipio^{1,4} and S R Arridge²

¹ Department of Applied Physics, University of Eastern Finland, PO Box 1627, 70211 Kuopio, Finland

² Department of Computer Science, University College London, Gower Street, London WC1E 6BT, UK

³ Department of Medical Physics and Bioengineering, University College London, Gower Street, London WC1E 6BT, UK

⁴ Department of Mathematics, University of Auckland, Private Bag 92019, Auckland Mail Centre, Auckland 1142, New Zealand

E-mail: tanja.tarvainen@uef.fi

Received 23 November 2011, in final form 21 May 2012

Published 30 July 2012

Online at stacks.iop.org/IP/28/084009

Abstract

Quantitative photoacoustic tomography is a novel hybrid imaging technique aiming at estimating optical parameters inside tissues. The method combines (functional) optical information and accurate anatomical information obtained using ultrasound techniques. The optical inverse problem of quantitative photoacoustic tomography is to estimate the optical parameters within tissue when absorbed optical energy density is given. In this paper we consider reconstruction of absorption and scattering distributions in quantitative photoacoustic tomography. The radiative transport equation and diffusion approximation are used as light transport models and solutions in different size domains are investigated. The simulations show that scaling of the data, for example by using logarithmic data, can be expected to significantly improve the convergence of the minimization algorithm. Furthermore, both the radiative transport equation and diffusion approximation can give good estimates for absorption. However, depending on the optical properties and the size of the domain, the diffusion approximation may not produce as good estimates for scattering as the radiative transport equation.

(Some figures may appear in colour only in the online journal)

1. Introduction

Photoacoustic tomography (PAT) is an emerging imaging modality developed over the past decade which combines the benefits of optical contrast and ultrasound propagation. The optical methods provide information about the distribution of chromophores which are light absorbing

molecules within the tissue. The chromophores of interest are, for example, haemoglobin and melanin. In addition, chromophores are utilized in tomographic contrast agent-based imaging in which case they are dyes, nanoparticles or genetically expressed markers that are used as contrast agents. The ultrasonic waves carry this optical information directly to the surface with minimal scattering, thus retaining accurate spatial information as well. Nowadays, PAT can be used to provide images of soft biological tissues with high spatial resolution. It has been successfully applied to the visualization of different structures in biological tissues such as human blood vessels, microvasculature of tumours and cerebral cortex in small animals. However, this information is only a qualitative image and it does not include information about the amount of chromophores. For more information about PAT, see e.g. [6, 33, 34] and references therein.

Quantitative photoacoustic tomography (QPAT) is a technique in which also the absolute concentration of chromophores is estimated. This is a hybrid imaging problem in which the solution of one inverse problem acts as a data for another ill-posed inverse problem.

In QPAT measurement situation, a short (ns) pulse of light is used to illuminate the region of tissue of interest. As light propagates within the tissue, it is absorbed by chromophores. This generates an increase in pressure and a small accompanying increase in temperature. Because of the elastic nature of tissue, the pressure increase propagates through the tissue as an acoustic wave and is detected by ultrasound sensors on the surface of the tissue. The propagation of the acoustic wave occurs on a microsecond timescale, about three orders of magnitude slower than the optical propagation, so only the total absorbed optical energy density is of interest and not the rate of absorption. This large difference in timescale allows the optical and acoustic parts of the inverse problem to be decoupled and treated separately.

The two inverse problems in QPAT are as follows: (i) reconstruct the initial acoustic pressure distribution from measured acoustic waves and (ii) reconstruct optical parameters from absorbed optical energy density. The first inverse problem (i) is an inverse initial value problem in acoustics. There are a large number of reconstruction techniques available [20, 33]. However, in cases in which the speed of sound or acoustic absorption within the tissue is varying, the inverse problem becomes significantly more challenging [13, 19, 31]. In this paper we consider the second inverse problem (ii). Furthermore, we assume that the Grüneisen coefficient which connects the acoustic pressure and absorbed optical energy density is known. For a discussion about the estimation of the Grüneisen coefficient simultaneously with optical parameters, see e.g. [3, 4, 27].

In the optical inverse problem of QPAT, the estimation of more than one optical parameter is non-unique if only one light source or optical wavelength is used. To overcome this problem, one approach has been to assume the scattering as known and estimate only the absorption [5, 8, 15, 23, 35, 36]. This, however, is unrealistic since in practical applications, scattering is usually not known. A different approach was taken in [24] where absorption and photon fluence were extracted using sparse signal representation. The two most commonly applied approaches to overcome the non-uniqueness problem when estimating more than one optical parameter simultaneously are as follows: a spectral approach in which more than one optical wavelength is used [9, 21, 4] and a multi-source QPAT in which multiple optical illuminations are used [3, 7, 11, 27, 37]. In this work we consider the latter approach.

Due to the ill posedness of the optical inverse problem of QPAT, the reconstruction is sensitive to the measurement and modelling errors. Therefore, light propagation within the target needs to be accurately modelled. The generally accepted model for light transport in tissues is the radiative transport equation (RTE) [14]. However, it is computationally expensive and therefore its applications in biomedical imaging have been limited. The most commonly applied model in biomedical imaging is the diffusion approximation (DA) to the RTE. It is

known to describe light propagation accurately in a diffusive regime, that is, sufficiently far from light source and when scattering is significantly larger than absorption [1, 14]. However, when these conditions are not fulfilled, it has been shown that the DA does not predict light propagation accurately [10, 22, 32] and the RTE needs to be used as a light propagation model.

Previously, the multi-source QPAT has been studied in [3] in which the DA was used as the forward model for light transport. In the approach, the absorption and diffusion coefficients were estimated from absorbed optical energy density. The results showed good reconstructions for both absorption and diffusion coefficients in a diffusive regime. The diffusive regime was considered also in [11] where absorption and reduced scattering coefficients were estimated using the DA as the light transport model. A non-iterative reconstruction technique for the estimation of absorption and diffusion perturbations in a diffusive regime was introduced in [27]. In [7] the estimation of absorption and scattering distributions in an inverse crime case was considered using both the RTE and the DA as light transport models. It was seen that the DA failed to give good estimates for scattering.

In this paper, we investigate a simultaneous estimation of absorption and scattering in multi-source QPAT. We consider both the RTE and the DA as light transport models and investigate the minimization problem in two size domains: in a transport regime and in a diffusive regime. The numerical solutions of the RTE and the DA are implemented using the finite element method (FEM). The image reconstruction is based on the nonlinear total variation regularized least-squares method in which scaling of the data and solution spaces are applied. Similar scaling has been applied in diffuse optical tomography [26, 28] and in QPAT [3, 11]. Furthermore, the total variation regularization has been applied for example in QPAT in [3, 7, 11]. The corresponding minimization problem is solved using the Gauss–Newton method.

The rest of this paper is organized as follows. The optical inverse problem of QPAT is described in section 2. The light transport models are reviewed in section 3 and finite element implementations are described in section 4. The simulation results are shown in section 5 and conclusions are given in section 6.

2. Optical inverse problem in QPAT

The optical inverse problem in QPAT is to estimate the optical properties of the object when absorbed optical energy density \mathcal{H} is given. In this paper, the estimated optical parameters are the absorption and scattering coefficients (μ_a, μ_s) within the medium.

We consider the solution of the inverse problem in a discrete framework. The domain Ω is discretized into K disjoint elements Ω_k , and the absorption and scattering coefficients are represented in basis

$$\mu_a(r) \approx \sum_{k=1}^K \mu_{a_k} \chi_k^{(\mu_a)}(r) \quad (1)$$

$$\mu_s(r) \approx \sum_{k=1}^K \mu_{s_k} \chi_k^{(\mu_s)}(r), \quad (2)$$

where $\chi_k(r)$ is a characteristic function of the element Ω_k . In general, let us use the notation $x := \begin{pmatrix} \mu_a \\ \mu_s \end{pmatrix}^T$ where $\mu_a = (\mu_{a,1}, \dots, \mu_{a,K})^T \in \mathbb{R}^K$ and $\mu_s = (\mu_{s,1}, \dots, \mu_{s,K})^T \in \mathbb{R}^K$ are vectors of projection coefficients in the approximations (1) and (2) for the absorption and scattering parameters. Furthermore, let the measurement vector be $\mathcal{H} = (\mathcal{H}_{1,1}, \dots, \mathcal{H}_{\ell,m})^T \in \mathbb{R}^{\ell \times m}$ where ℓ is the number of illuminations and m is the number of measurements (measurement pixels).

The regularized nonlinear least-squares problem is to estimate the absorption and scattering distributions \hat{x} which minimize the functional

$$\hat{x} = \arg \min_x \{ \|L_e(\mathcal{H} - \mathcal{F}(x))\|^2 + \mathcal{B}(x) \} \quad (3)$$

when the measured data \mathcal{H} are given. In (3), \mathcal{F} is the forward model for light transport which maps the absorption and scattering parameters to the data. In this work, we use two models, the RTE and the DA, as forward models. Furthermore, matrix L_e is a weighting matrix which, from the statistical point of view, can be interpreted as the Cholesky factor of the inverse of the noise covariance matrix. The term $\mathcal{B}(x) > 0$ is a regularizing penalty functional. Regularization is needed to overcome the instability that is due to the ill-posed nature of the problem. In this paper, we use a total variation prior for regularization. The total variation norm is a good prior for piecewise constant images which consists of a few constant levels with relatively short boundary lines [18]. In this paper, it is constructed similarly as in [18, 28] for the diffuse optical tomography. Previously, it has been applied in QPAT, for example, in [3, 7, 11].

In QPAT, where the dynamic range of the measured light intensities can be very large, scaling of the data may be needed in order to ensure numerical stability of the optimization problem. Furthermore, transformation of the solution space may be used to constitute a correct preconditioning. In this work, the data space is scaled similarly as in [26, 28] in the case of the diffuse optical tomography, thus

$$\tilde{\mathcal{H}} = \ln \mathcal{H}; \quad (4)$$

thus, we use the logarithm of amplitude as the data. Furthermore, in the solution space the absorption and scattering values are scaled with their mean values as

$$\tilde{\mu}_a = \frac{\mu_a}{\bar{\mu}_a}, \quad \tilde{\mu}_s = \frac{\mu_s}{\bar{\mu}_s}, \quad (5)$$

where $\bar{\mu}_a$ and $\bar{\mu}_s$ are the mean of the absorption and scattering, respectively. Thus, taking into account the scaling, the minimization problem is of the form

$$\hat{x} = \arg \min_{\tilde{x}} \{ \|L_{\tilde{e}}(\tilde{\mathcal{H}} - \mathcal{F}(\tilde{x}))\|^2 + \mathcal{B}(\tilde{x}) \}, \quad (6)$$

where $\tilde{x} := (\tilde{\mu}_a, \tilde{\mu}_s)^T$.

In this work the minimization problem (6) is solved using the Gauss–Newton method which is equipped with a line search algorithm for the determination of the step length and a positivity constraint for the estimated parameters. The main reason for the choice of this minimization approach is that it was found to produce best convergence in the challenging situations in which the DA does not have a clear minimum. Examples of this are shown later in section 5. However, the construction of the Jacobian is time consuming and other approaches such as gradient-based methods will be considered in the future. Gauss–Newton iteration for the solution of (6) is of the form

$$\tilde{x}_{(i+1)} = \tilde{x}_{(i)} + s_{(i)} \left(\tilde{J}_{(i)}^T W \tilde{J}_{(i)} + \frac{1}{2} H_B(\tilde{x}_{(i)}) \right)^{-1} \left(\tilde{J}_{(i)}^T W (\tilde{\mathcal{H}} - \mathcal{F}(\tilde{x}_{(i)})) - \frac{1}{2} g_B(\tilde{x}_{(i)}) \right), \quad (7)$$

where i is the iteration index, $s_{(i)}$ is a step length parameter which is determined by the line search algorithm, \tilde{J} is the Jacobian and $W = L_{\tilde{e}}^T L_{\tilde{e}}$. Furthermore, $H_B(\tilde{x})$ and $g_B(\tilde{x})$ are the Hessian and gradient of the penalty functional. The computation of the Jacobian is explained in more detail in section 4.3.

3. Modelling light transport

The optical forward problem in QPAT is to compute the absorbed optical energy density when the optical properties of the medium and the input light sources are given. Light

propagation in biological media is usually modelled through transport theory which can be treated through stochastic methods, such as Monte Carlo, or deterministic methods which are based on describing particle transport with integro-differential equations. In the following we consider the latter approach.

3.1. Radiative transport equation

A widely accepted model for light transport in tissues is the RTE [14]. The RTE is a one-speed approximation of the transport equation, and thus it assumes that the energy (or speed) of the particles does not change in collisions and that the refractive index is constant within the medium.

Let $\Omega \subset \mathbb{R}^n$, $n = 2$ or 3 denote the physical domain with boundary $\partial\Omega$ and let $\hat{s} \in S^{n-1}$ denote a unit vector in the direction of interest. In QPAT, we use the time-independent RTE

$$\hat{s} \cdot \nabla \phi(r, \hat{s}) + (\mu_s + \mu_a)\phi(r, \hat{s}) = \mu_s \int_{S^{n-1}} \Theta(\hat{s} \cdot \hat{s}') \phi(r, \hat{s}') d\hat{s}' + q(r, \hat{s}), \quad r \in \Omega, \quad (8)$$

where $\mu_s = \mu_s(r)$ and $\mu_a = \mu_a(r)$ are the scattering and absorption coefficients of the medium, respectively, $\phi(r, \hat{s})$ is the radiance, $\Theta(\hat{s} \cdot \hat{s}')$ is the scattering phase function and $q(r, \hat{s})$ is the source inside Ω .

The scattering phase function $\Theta(\hat{s} \cdot \hat{s}')$ describes the probability that a photon with an initial direction \hat{s}' will have a direction \hat{s} after a scattering event. In biological tissues, the most commonly used phase function is the Henyey–Greenstein scattering function [12] which is of the form

$$\Theta(\hat{s} \cdot \hat{s}') = \begin{cases} \frac{1}{2\pi} \frac{1 - g^2}{(1 + g^2 - 2g\hat{s} \cdot \hat{s}')}, & n = 2 \\ \frac{1}{4\pi} \frac{1 - g^2}{(1 + g^2 - 2g\hat{s} \cdot \hat{s}')^{3/2}}, & n = 3. \end{cases} \quad (9)$$

The anisotropy parameter g defines the shape of the probability density and it obtains values between $-1 < g < 1$. With the value $g = 0$, the scattering probability density is a uniform distribution. For forward dominated scattering $g > 0$ and for backward dominated scattering $g < 0$.

In QPAT, we use the RTE boundary condition which assumes that no photons travel in an inward direction at the boundary $\partial\Omega$ except at source position $\epsilon_j \subset \partial\Omega$, thus

$$\phi(r, \hat{s}) = \begin{cases} \phi_0(r, \hat{s}), & r \in \epsilon_j, \quad \hat{s} \cdot \hat{n} < 0 \\ 0, & r \in \partial\Omega \setminus \epsilon_j, \quad \hat{s} \cdot \hat{n} < 0, \end{cases} \quad (10)$$

where \hat{n} is an outward unit normal and $\phi_0(r, \hat{s})$ is a boundary source [1, 30]. This boundary condition implies that once a photon escapes the domain Ω , it does not re-enter it.

The absorbed optical energy density $H(r)$ can be solved as

$$H(r) = \mu_a \Phi(r), \quad (11)$$

where $\Phi(r)$ is the fluence which is defined as

$$\Phi(r) = \int_{S^{n-1}} \phi(r, \hat{s}) d\hat{s}. \quad (12)$$

3.2. Diffusion approximation

In the DA framework, the radiance is approximated by

$$\phi(r, \hat{s}) \approx \frac{1}{|S^{n-1}|} \Phi(r) - \frac{n}{|S^{n-1}|} \hat{s} \cdot (\kappa \nabla \Phi(r)), \quad (13)$$

where $\kappa = (n(\mu_a + \mu'_s))^{-1}$ is the diffusion coefficient where $\mu'_s = (1 - g_1)\mu_s$ is the reduced scattering coefficient and g_1 is the mean of the cosine of the scattering angle [1, 16]. In the case of the Henyey–Greenstein scattering function, equation (9), we have $g_1 = g$. By inserting the approximation (13) and similar approximations written for the source term and phase function into equation (8) and following the derivation in [1, 14], we obtain the DA

$$-\nabla \cdot \kappa \nabla \Phi(r) + \mu_a \Phi(r) = q_0(r), \quad r \in \Omega, \quad (14)$$

where $q_0(r)$ is the source inside Ω .

The boundary condition (10) cannot be expressed in terms of variables of the DA. Instead, it is often replaced by an approximation that the total inward directed photon current is zero. Furthermore, by taking into account the mismatch between the refractive indices of the medium and surrounding medium, a Robin-type boundary condition can be derived; see for example [1]. This boundary condition can be written as

$$\Phi(r) + \frac{1}{2\gamma_n} \kappa A \frac{\partial \Phi(r)}{\partial \hat{n}} = \begin{cases} \frac{I_s}{\gamma_n}, & r \in \epsilon_i \\ 0, & r \in \partial\Omega \setminus \epsilon_i, \end{cases} \quad (15)$$

where I_s is a diffuse boundary current at the source position $\epsilon_j \subset \partial\Omega$, γ_n is a dimension-dependent constant which takes values $\gamma_2 = 1/\pi$ and $\gamma_3 = 1/4$ and A is a parameter governing the internal reflection at the boundary $\partial\Omega$ [16]. In the case of matched refractive index, $A = 1$.

4. Finite element implementations

In this work, the FEM is used for the solution of the RTE and the DA. In the FEM, a variational formulation is derived for the original problem. Then, a finite-dimensional approximation for the variational formulation is constructed using a suitably chosen basis and test functions in the solution space.

4.1. FE approximation of the RTE

In this work, the FE approximation of the RTE (8) with boundary condition (10) is derived and implemented similarly as in [28, 29]. Thus, both the spatial and angular discretizations are implemented in piecewise linear bases. As a result, a following matrix equation is obtained

$$A_{\text{rte}} \alpha = b_{\text{rte}}, \quad (16)$$

where $\alpha = (\alpha_{1,1}, \dots, \alpha_{1,N_\theta}, \alpha_{2,1}, \dots, \alpha_{2,N_\theta}, \dots, \alpha_{N_n,1}, \dots, \alpha_{N_n,N_\theta})^T \in \mathbb{R}^{N_n N_\theta}$ is the radiance in nodal points of the spatial and angular meshes, N_n is the number of spatial nodes and N_θ is the number of angular directions. Furthermore, $b_{\text{rte}} = b\psi^0$ where ψ^0 is the source strength vector, and $A_{\text{rte}} = A_1 + A_2 + A_3 + A_4$ where

$$A_1(h, s) = - \int_{\Omega} \int_{S^{n-1}} \hat{s} \cdot \nabla \psi_j(r) \psi_m(\hat{s}) \psi_\ell(\hat{s}) d\hat{s} \psi_i(r) dr \\ + \int_{\Omega} \delta \int_{S^{n-1}} (\hat{s} \cdot \nabla \psi_j(r) \psi_m(\hat{s})) (\hat{s} \cdot \nabla \psi_i(r) \psi_\ell(\hat{s})) d\hat{s} dr \quad (17)$$

$$A_2(h, s) = \int_{\partial\Omega} \psi_i(r) \psi_j(r) dS \int_{S^{n-1}} (\hat{s} \cdot \hat{n})_+ \psi_\ell(\hat{s}) \psi_m(\hat{s}) d\hat{s} \quad (18)$$

$$A_3(h, s) = \int_{\Omega} (\mu_s + \mu_a) \psi_i(r) \psi_j(r) \, dr \int_{S^{n-1}} \psi_{\ell}(\hat{s}) \psi_m(\hat{s}) \, d\hat{s} \\ + \int_{\Omega} \delta(\mu_s + \mu_a) \int_{S^{n-1}} \hat{s} \cdot \nabla \psi_j(r) \psi_m(\hat{s}) \psi_{\ell}(\hat{s}) \, d\hat{s} \psi_i(r) \, dr \quad (19)$$

$$A_4(h, s) = - \int_{\Omega} \mu_s \psi_i(r) \psi_j(r) \, dr \int_{S^{n-1}} \int_{S^{n-1}} \Theta(\hat{s} \cdot \hat{s}') \psi_{\ell}(\hat{s}') \, d\hat{s}' \psi_m(\hat{s}) \, d\hat{s} \\ - \int_{\Omega} \delta \mu_s \int_{S^{n-1}} \hat{s} \cdot \nabla \psi_j(r) \psi_m(\hat{s}) \int_{S^{n-1}} \Theta(\hat{s} \cdot \hat{s}') \psi_{\ell}(\hat{s}') \, d\hat{s}' \, d\hat{s} \psi_i(r) \, dr \quad (20)$$

$$b(h, s) = \int_{\partial\Omega} \psi_i(r) \psi_j(r) \, dS \int_{S^{n-1}} (\hat{s} \cdot \hat{n})_- \psi_{\ell}(\hat{s}) \psi_m(\hat{s}) \, d\hat{s}, \quad (21)$$

where $h = N_{\theta}(j-1) + m$, $s = N_{\theta}(i-1) + \ell$ ($j, i = 1, \dots, N_n$, $m, \ell = 1, \dots, N_{\theta}$, $h, s = 1, \dots, N_n N_{\theta}$), $\psi_i(r)$ and $\psi_j(r)$ are spatial basis functions, $\psi_{\ell}(r)$ and $\psi_m(r)$ are angular basis functions and δ is a streamline diffusion modification parameter [17, 28]. The FE solution of the RTE is obtained using equation (16). Thus, as a solution, the radiance α in nodes of the spatial and angular discretizations is obtained. Then, the absorbed optical energy density can be calculated using equations (11) and (12).

4.2. FE approximation of the DA

In this work, the FE solution of the DA (14) with the boundary condition (15) is implemented similarly as in [2]. Thus, the FE solution of the DA is obtained as a solution of the following matrix equation:

$$A_{\text{da}} a = b_{\text{da}}, \quad (22)$$

where $A_{\text{da}} = K + C + R$ and

$$K(p, q) = \int_{\Omega} \kappa \nabla \varphi_q(r) \cdot \nabla \varphi_p(r) \, dr \quad (23)$$

$$C(p, q) = \int_{\Omega} \mu_a \varphi_q(r) \varphi_p(r) \, dr \quad (24)$$

$$R(p, q) = \int_{\partial\Omega} \frac{2\gamma_n}{A} \varphi_q(r) \varphi_p(r) \, dS \quad (25)$$

$$b_{\text{da}}(p) = \int_{\epsilon_i} \frac{2I_s}{A} \varphi_p(r) \, dS, \quad (26)$$

where $q, p = 1, \dots, N$, $\varphi_q(r)$ and $\varphi_p(r)$ are basis functions, and N is the number of nodes. As a solution of the DA, fluence a in the nodes of the FE mesh is obtained and the absorbed optical energy density can be calculated using equation (11).

4.3. Jacobian

In the Gauss–Newton algorithm, the Jacobian needs to be computed on each iteration. Taking into account the scaling described in section 2, the scaled Jacobian $\tilde{J} = (\tilde{J}_{\mu_a}, \tilde{J}_{\mu_s})$ is of the form

$$\tilde{J}_{\mu_a} = \text{diag}(\mathcal{F})^{-1} J_{\mu_a} \bar{\mu}_a \quad (27)$$

$$\tilde{J}_{\mu_s} = \text{diag}(\mathcal{F})^{-1} J_{\mu_s} \bar{\mu}_s, \quad (28)$$

where \mathcal{F} is the forward model.

In the case of the RTE, the k th column of the Jacobian for absorption $J_{\mu_a, \text{RTE}}$ and scattering $J_{\mu_s, \text{RTE}}$ corresponding to element Ω_k is obtained by a column-wise vectorization of

$$j_{\mu_a, \text{RTE}}^{(k)} = -\mu_a^{(k)} \mathcal{M}_{\text{rte}} A_{\text{rte}}^{-1} \frac{\partial A_{\text{rte}}}{\partial \mu_{a_k}} A_{\text{rte}}^{-1} b_{\text{rte}} + \chi_k \mathcal{M}_{\text{rte}} A_{\text{rte}}^{-1} b_{\text{rte}} \quad (29)$$

$$j_{\mu_s, \text{RTE}}^{(k)} = -\mu_a^{(k)} \mathcal{M}_{\text{rte}} A_{\text{rte}}^{-1} \frac{\partial A_{\text{rte}}}{\partial \mu_{s_k}} A_{\text{rte}}^{-1} b_{\text{rte}}, \quad (30)$$

where

$$\frac{\partial A_{\text{rte}}}{\partial \mu_{a_k}}(h, s) = \int_{\Omega_k} \psi_i(r) \psi_j(r) \, dr \int_{S^{n-1}} \psi_\ell(\hat{s}) \psi_m(\hat{s}) \, d\hat{s} \quad (31)$$

$$\begin{aligned} \frac{\partial A_{\text{rte}}}{\partial \mu_{s_k}}(h, s) = & \int_{\Omega_k} \psi_i(r) \psi_j(r) \, dr \int_{S^{n-1}} \psi_\ell(\hat{s}) \psi_m(\hat{s}) \, d\hat{s} \\ & - \int_{\Omega_k} \psi_i(r) \psi_j(r) \, dr \int_{S^{n-1}} \int_{S^{n-1}} \Theta(\hat{s} \cdot \hat{s}') \psi_\ell(\hat{s}') \, d\hat{s}' \psi_m(\hat{s}) \, d\hat{s} \end{aligned} \quad (32)$$

and \mathcal{M}_{rte} is a discretized measurement operator for the RTE.

In the case of the DA, the k th column of Jacobian for absorption $J_{\mu_a, \text{DA}}$ and scattering $J_{\mu_s, \text{DA}}$ corresponding to element Ω_k is obtained by a column-wise vectorization of

$$j_{\mu_a, \text{DA}}^{(k)} = -\mu_a^{(k)} \mathcal{M}_{\text{da}} A_{\text{da}}^{-1} \frac{\partial A_{\text{da}}}{\partial \mu_{a_k}} A_{\text{da}}^{-1} b_{\text{da}} + \chi_k \mathcal{M}_{\text{da}} A_{\text{da}}^{-1} b_{\text{da}} \quad (33)$$

$$j_{\mu_s, \text{DA}}^{(k)} = -\mu_a^{(k)} \mathcal{M}_{\text{da}} A_{\text{da}}^{-1} \frac{\partial A_{\text{da}}}{\partial \mu_{s_k}} A_{\text{da}}^{-1} b_{\text{da}}, \quad (34)$$

where

$$\frac{\partial A_{\text{da}}}{\partial \mu_{a_k}}(p, q) = -\frac{1}{n(\mu_{a_k} + (1-g)\mu_{s_k})^2} \int_{\Omega_k} \nabla \varphi_q(r) \cdot \nabla \varphi_p(r) \, dr + \int_{\Omega_k} \varphi_q(r) \varphi_p(r) \, dr \quad (35)$$

$$\frac{\partial A_{\text{da}}}{\partial \mu_{s_k}}(p, q) = -\frac{1-g}{n(\mu_{a_k} + (1-g)\mu_{s_k})^2} \int_{\Omega_k} \nabla \varphi_q(r) \cdot \nabla \varphi_p(r) \, dr \quad (36)$$

and \mathcal{M}_{da} is a discretized measurement operator for the DA.

5. Simulation results

The optical inverse problem of QPAT was investigated with simulations. We were interested in estimating both absorption and scattering in different size domains using both the RTE and the DA as light transport models. The FEM was used for numerical implementations. Two rectangular domains were considered. The size of the smaller domain was 4 mm \times 8 mm. According to theory, light transport within it is accurately modelled with the RTE but not with the DA. The size of the larger domain was 20 mm \times 40 mm. It can be considered to be in a diffusive regime, and thus both RTE and DA can be expected to be suitable light transport models. In all of the simulations, four illuminations, one at each side of the rectangle, were used.

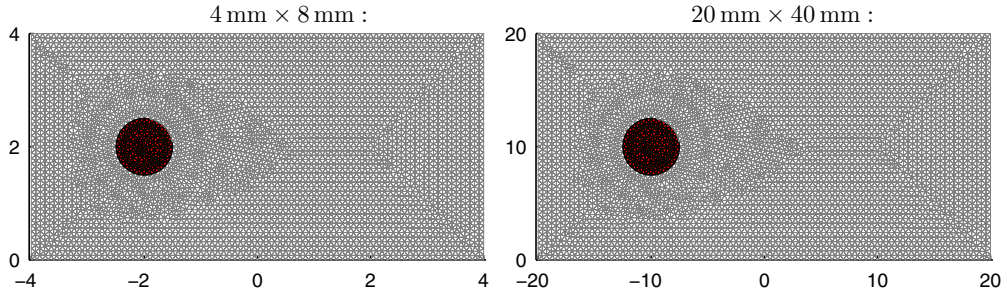


Figure 1. Mesh geometry and position of the perturbation in a single perturbation case in a $4 \text{ mm} \times 8 \text{ mm}$ domain (left image) and in a $20 \text{ mm} \times 40 \text{ mm}$ domain (right image).

5.1. Error surfaces for a single perturbation case

To illustrate the reconstruction problem of a simultaneous estimation of absorption and scattering, we considered a simple problem of single perturbation located within homogeneous and known background similarly as was done in [25] in the case of diffuse optical tomography. For this case, we can plot Ψ as a function of $\mu_a^{(P)}$ and $\mu_s^{(P)}$.

$$\Psi(\mu_a^{(P)}, \mu_s^{(P)}) = \|\mathcal{F}(\mu_{a,\text{ref}}^{(P)}, \mu_{s,\text{ref}}^{(P)}) - \mathcal{F}(\mu_a^{(P)}, \mu_s^{(P)})\|^2, \quad (37)$$

where $\mathcal{F}(\mu_{a,\text{ref}}^{(P)}, \mu_{s,\text{ref}}^{(P)})$ is the reference data vector obtained with perturbation values $\mu_{a,\text{ref}}^{(P)}$ and $\mu_{s,\text{ref}}^{(P)}$. The background parameters $(\mu_a^{(B)}, \mu_s^{(B)})$ were kept fixed at correct values.

Case 1. $4 \text{ mm} \times 8 \text{ mm}$ domain:

First, the small domain of size $4 \text{ mm} \times 8 \text{ mm}$ was considered. The perturbation was a circular inclusion with radius of $r = 0.5 \text{ mm}$. We used constant background parameters $\mu_a^{(B)} = 0.01 \text{ mm}^{-1}$ and $\mu_s^{(B)} = 2 \text{ mm}^{-1}$. Furthermore, the anisotropy parameter was constant $g = 0.8$. The reference data set was generated with perturbation parameters $\mu_{a,\text{ref}}^{(P)} = 0.02 \text{ mm}^{-1}$ and $\mu_{s,\text{ref}}^{(P)} = 4 \text{ mm}^{-1}$. The test data were generated for all combinations for 20 absorption $\mu_a^{(P)}$ values in the range from 0.001 to 0.1 mm^{-1} and 20 scattering $\mu_s^{(P)}$ values in the range from 0.1 to 20 mm^{-1} . Both the RTE and the DA were used as light transport models. In the FE implementation, the spatial FE discretization consisted of 8638 triangular elements and 4440 nodes. Furthermore, the angular discretization of the RTE consisted of 64 angles. The mesh geometry and the perturbation are shown in the left image of figure 1.

The graphs in figure 2 show maps of $\Psi(\mu_a^{(P)}, \mu_s^{(P)})$ for absorbed optical energy density H and logarithm of absorbed optical energy density $\ln(H)$. On the first row, the reference data and test data sets were generated using the RTE. On the second row, the reference data and test data sets were generated using the DA. All data sets were calculated in the same mesh and no noise was added. Therefore, all error maps reach their absolute minimum of zero at the correct perturbation data set.

Comparing the graphs shows that using absorbed optical energy density H as a data type gives much longer minimum ‘valley’ in the direction of scattering compared to logarithm of absorbed optical energy density $\ln(H)$. This indicates that scaling of the data for example by taking the logarithm can improve the convergence of the minimization algorithm significantly. Furthermore, when the results computed using the RTE and the DA are compared, it can be seen that graphs obtained using the RTE as the forward model show a clearer minimum (when scattering is varied) than when the DA is used. Thus, the reconstruction of scattering using

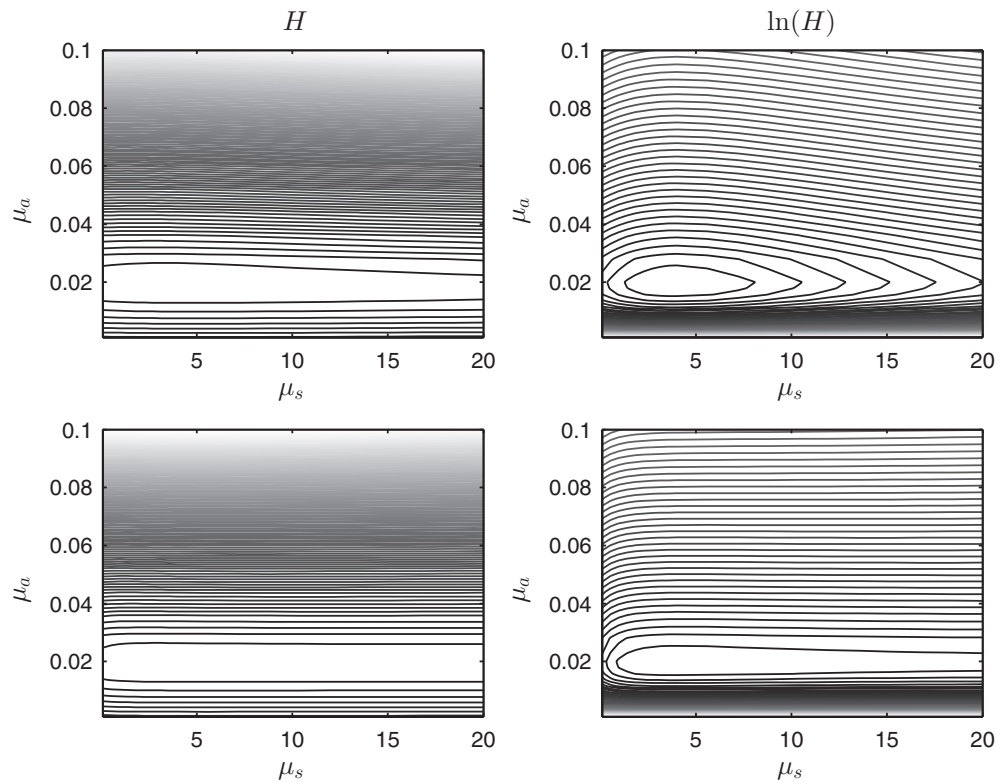


Figure 2. Objective functions for a single perturbation case in a $4\text{ mm} \times 8\text{ mm}$ domain as a function of scattering coefficient and absorption coefficient of the perturbation. The data types are the absorbed optical energy density H (left column) and logarithm of absorbed optical energy density $\ln(H)$ (right column). The RTE results are on the top row and the DA results are on the bottom row.

the DA is more ill posed than using the RTE. This indicates that in small domains, the DA is likely not to give as reliable estimates for scattering as the RTE.

Case 2. $20\text{ mm} \times 40\text{ mm}$ domain:

Then, the larger domain of size $20\text{ mm} \times 40\text{ mm}$ was considered. The perturbation was a circular inclusion with radius of $r = 2.5\text{ mm}$. We used the same optical parameters as in the smaller domain. Thus, background parameters were $\mu_a^{(B)} = 0.01\text{ mm}^{-1}$ and $\mu_s^{(B)} = 2\text{ mm}^{-1}$, and the anisotropy parameter was constant $g = 0.8$. The reference data set was generated with perturbation parameters $\mu_{a,\text{ref}}^{(P)} = 0.02\text{ mm}^{-1}$ and $\mu_{s,\text{ref}}^{(P)} = 4\text{ mm}^{-1}$, and the test data were generated for all combinations for 20 absorption $\mu_a^{(P)}$ values in the range from 0.001 to 0.1 mm^{-1} and 20 scattering $\mu_s^{(P)}$ values in the range from 0.1 mm^{-1} to 20 mm^{-1} . Again, both the RTE and the DA were considered. The spatial FE discretization consisted of 8640 triangular elements and 4441 nodes, and the angular discretization of the RTE consisted of 64 directions. The mesh geometry and the perturbation are shown in the right image of figure 1.

The graphs in figure 3 show maps of $\Psi(\mu_a^{(P)}, \mu_s^{(P)})$ for absorbed optical energy density H and logarithm of absorbed optical energy density $\ln(H)$ calculated in the larger domain. On the first row, the reference data and test data sets were generated using the RTE and on the

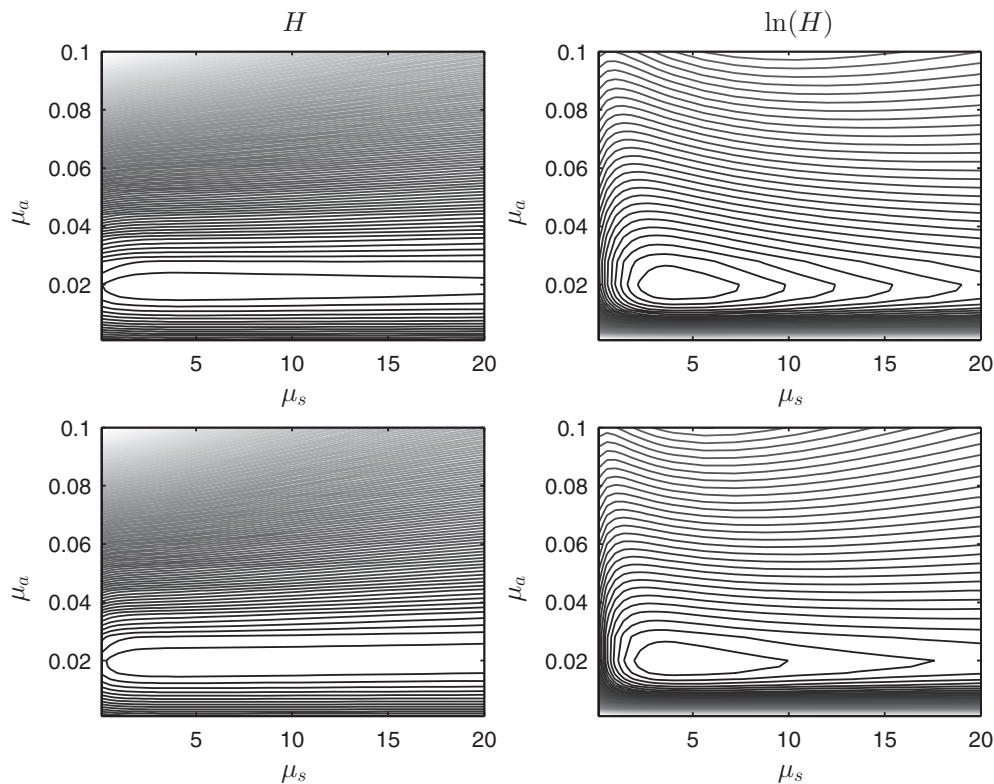


Figure 3. Objective functions for a single perturbation case in a $20\text{ mm} \times 40\text{ mm}$ domain as a function of scattering coefficient and absorption coefficient of the perturbation. The data types are the absorbed optical energy density H (left column) and logarithm of absorbed optical energy density $\ln(H)$ (right column). The RTE results are on the top row and the DA results are on the bottom row.

second row, the DA was used. Again, all data sets were calculated in the same mesh and no noise was added.

Comparing the graphs obtained using the absorbed optical energy density H and logarithm of absorbed optical energy density $\ln(H)$ as data types shows again the similar minimum ‘valley’ as in the smaller domain. This indicates that also in the larger domain, logarithmic data (or other similar scaling) are likely to give faster convergence of the minimization algorithm. Comparing the RTE and DA results shows that now they both show a clear minimum. This indicates that the RTE and DA can give the same quality reconstructions in a diffusive regime.

5.2. Reconstructions

To test the feasibility of the RTE and the DA to estimate absorption and scattering parameters, we performed reconstructions in two same-sized domains as in the single perturbation case. The simulation domains consisted of heterogeneous optical properties with varying and partially overlapping absorption and scattering inclusions. The optical parameters were chosen to be on a typical range of biological tissues and also low-scattering regions were included. The purpose was to simulate the method with tissue-like optical properties and to see how well absorption and scattering values can be distinguished also in cases in which they do not correlate.

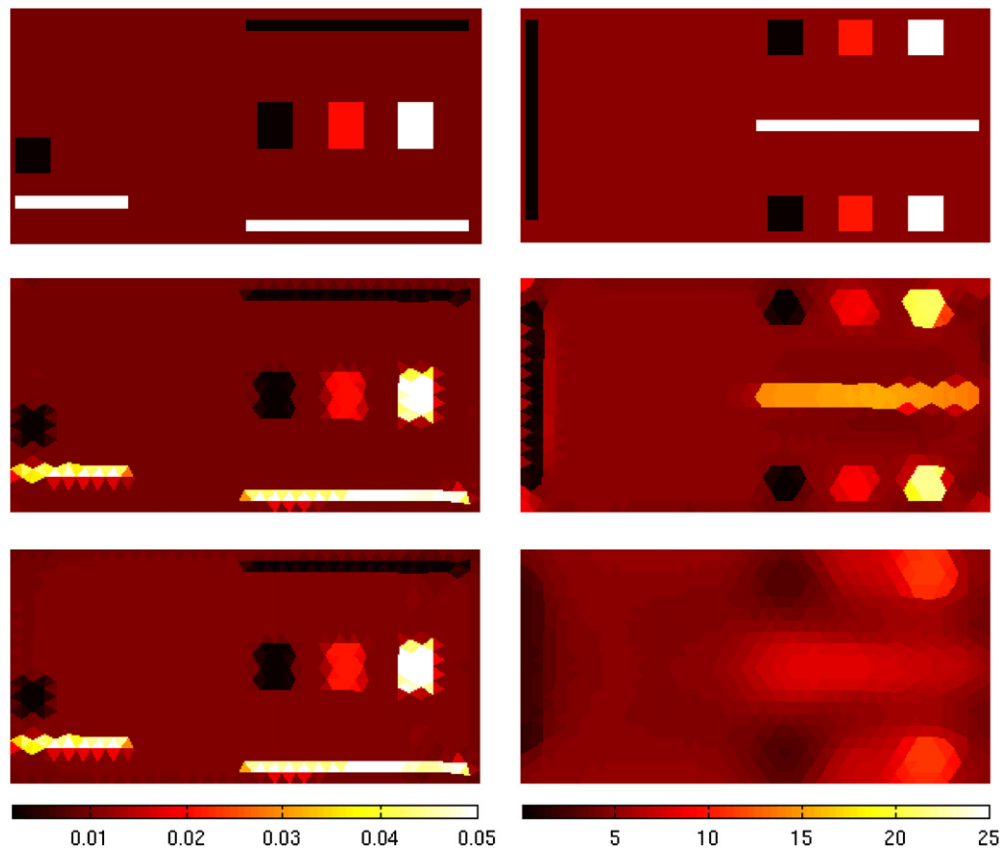


Figure 4. Reconstructed absorption (left column) and scattering (right column) distributions in a $4\text{ mm} \times 8\text{ mm}$ domain. Rows from top to bottom: the simulated distributions (first row), RTE reconstructions (second row) and DA reconstructions (third row).

Case 1. $4\text{ mm} \times 8\text{ mm}$ domain:

First, the small domain of size $4\text{ mm} \times 8\text{ mm}$ was considered. The distributions of simulated absorption and scattering values are shown on the top row of figure 4. The anisotropy parameter was $g = 0.8$ throughout the domain. The data were simulated using the RTE which was solved using the FEM. The FE discretization of the domain consisted of 9322 triangular elements and 4782 nodes. The angular discretization consisted of 128 directions. Gaussian distributed noise with standard deviation of 1% of the corresponding amplitude was added to the data.

The absorption and scattering distributions were reconstructed from the simulated data as described in section 2 by minimizing functional (6). Thus, the logarithm of absorbed optical energy density was chosen as the data type. The data were represented in a piece-wise constant basis using 1308 triangles. The same triangularization was used for the representation of the absorption and scattering in a piece-wise constant basis (1), (2) where $K = 1308$. The forward models used in reconstructions were the RTE and the DA. The discretization mesh consisted of 1308 triangular elements and 703 nodes. In the case of the RTE, 64 angular directions were used.

The reconstructed absorption and scattering distributions are shown in figure 4. Furthermore, the cross-sections through absorption and scattering distributions at y -positions $y = 3.7\text{ mm}$, $y = 2\text{ mm}$ and $y = 0.3\text{ mm}$ are shown in figure 5. In order to compare the

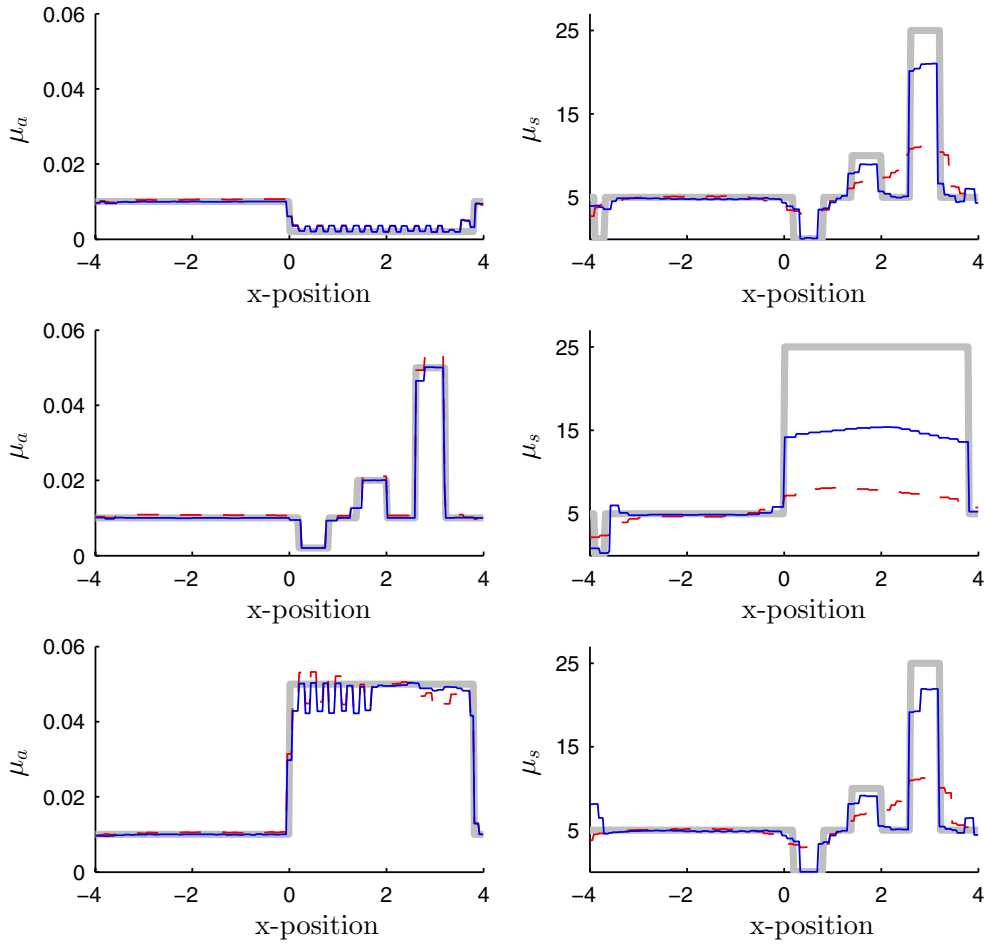


Figure 5. Cross-sections through absorption (left column) and scattering (right column) distributions in a 4 mm \times 8 mm domain at y -positions: $y = 3.7$ mm (first row), $y = 2$ mm (second row) and $y = 0.3$ mm (third row). The simulated distributions (thick grey line), the RTE solutions (solid blue line) and the DA solutions (dashed red line).

accuracy of the estimated parameters obtained using the RTE and the DA as light transport models, we calculated the estimation errors. The estimation errors for absorption \tilde{e}_{μ_a} and scattering \tilde{e}_{μ_s} were calculated as

$$\tilde{e}_{\mu_a} = \frac{\int_{\Omega} (\mu_a - \hat{\mu}_a)^2 d\Omega}{\int_{\Omega} \mu_a^2 d\Omega} \cdot 100, \quad \tilde{e}_{\mu_s} = \frac{\int_{\Omega} (\mu_s - \hat{\mu}_s)^2 d\Omega}{\int_{\Omega} \mu_s^2 d\Omega} \cdot 100 \quad (38)$$

where μ_a and μ_s are the original absorption and scattering coefficients and $\hat{\mu}_a$ and $\hat{\mu}_s$ are the estimated values. In this paper we wanted in particular to compare the errors that arise between the two models. The estimation errors are given in table 1.

As can be seen, the reconstructions obtained using the RTE as the forward model are similar to the original optical parameter distributions for both absorption and scattering. The DA gives as good reconstructions for absorption as the RTE. The scattering reconstructions obtained with the DA, however, are unclear and the estimated parameters differ from the original ones. This can also be noted from the estimation errors in table 1 where the estimation errors of absorption obtained with the RTE and the DA are of the same magnitude but the

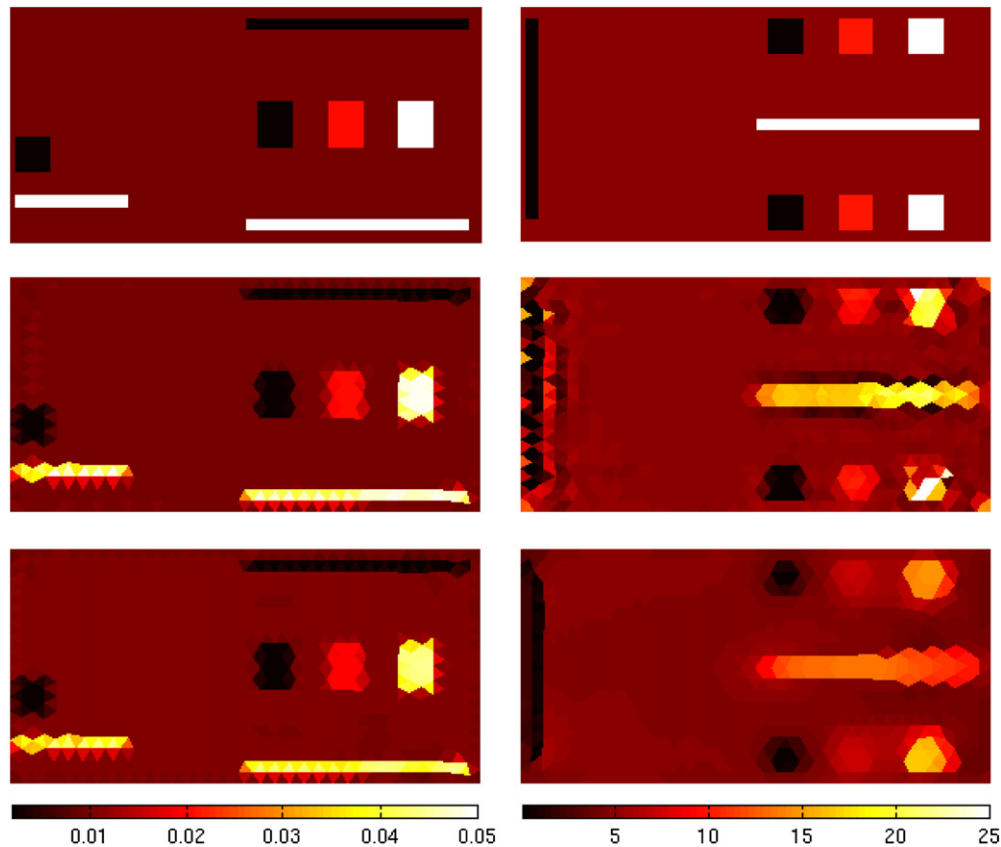


Figure 6. Reconstructed absorption (left column) and scattering (right column) distributions in a $20\text{ mm} \times 40\text{ mm}$ domain. Rows from top to bottom: the simulated distributions (first row), RTE reconstructions (second row) and DA reconstructions (third row).

Table 1. Estimation errors of absorption \tilde{e}_{μ_a} (%) and scattering \tilde{e}_{μ_s} (%) calculated for the RTE and the DA in domains ($4\text{ mm} \times 8\text{ mm}$) and ($20\text{ mm} \times 40\text{ mm}$).

	$4\text{ mm} \times 8\text{ mm}$		$20\text{ mm} \times 40\text{ mm}$	
	\tilde{e}_{μ_a}	\tilde{e}_{μ_s}	\tilde{e}_{μ_a}	\tilde{e}_{μ_s}
RTE	3.9	13.0	3.4	17.2
DA	4.1	26.7	3.5	17.3

estimation errors of scattering are larger for the DA than for the RTE. Thus in a small domain, both the RTE and DA can produce estimates for absorption with the same accuracy. However, the scattering estimates obtained with the DA are not as accurate as with the RTE.

Case 2. $20\text{ mm} \times 40\text{ mm}$ domain:

The distributions of simulated absorption and scattering values in the larger domain of size $20\text{ mm} \times 40\text{ mm}$ are shown on the top row of figure 6. The anisotropy parameter was $g = 0.8$. Again, the RTE was used to simulate the data. The spatial FE discretization consisted of 9224 triangular elements and 4733 nodes. Furthermore, the angular discretization consisted

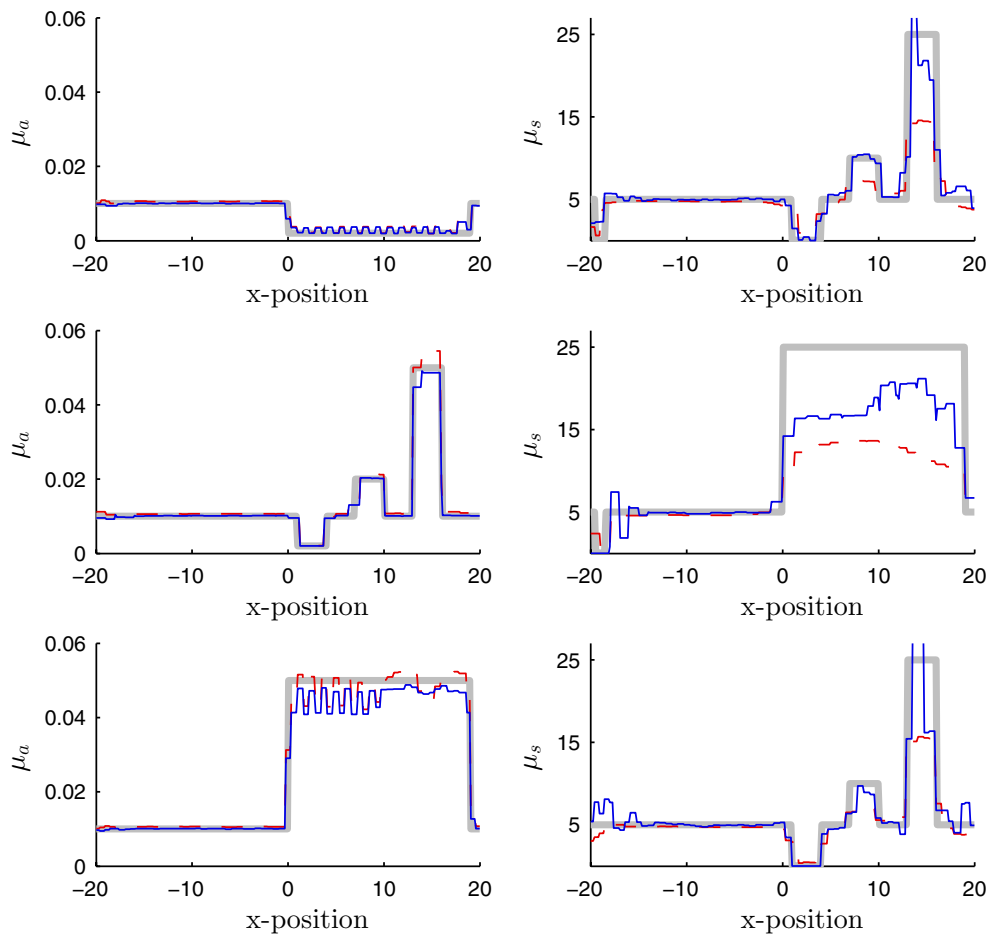


Figure 7. Cross-sections through absorption (left column) and scattering (right column) distributions in a 20 mm \times 40 mm domain at y -positions: $y = 18.5$ mm (first row), $y = 10$ mm (second row) and $y = 1.5$ mm (third row). The simulated distributions (thick grey line), the RTE solutions (solid blue line) and the DA solutions (dashed red line).

of 128 angular directions. Gaussian distributed noise with standard deviation of 1% of the corresponding amplitude was added to the data.

The absorption and scattering distributions were reconstructed similarly as in the smaller domain by minimizing functional (6) and using the logarithm of absorbed optical energy density as the data type. The data were represented in a piece-wise constant basis using 1308 triangles, and the same triangularization was used for the representation of the absorption and scattering in a piece-wise constant basis (1), (2). Both the RTE and the DA were used as forward models. The discretization mesh consisted of 1308 triangular elements and 703 nodes. In the case of the RTE, 64 angular directions were used.

The reconstructed absorption and scattering distributions are shown in figure 6 and the cross-sections through absorption and scattering distributions at y -positions $y = 18.5$ mm, $y = 10$ mm and $y = 1.5$ mm are shown in figure 7. The relative estimation errors calculated using equations (38) are given in table 1. As can be seen, in the large domain, the reconstructions

obtained using both the RTE and the DA as forward models are similar to the original optical parameter distribution for both absorption and scattering. Also the relative estimation errors are of the same magnitude when comparing results between the RTE and DA models. Thus, in a diffusive regime, both the RTE and DA can produce absorption and scattering estimates of the same accuracy.

6. Conclusions

In this work the optical inverse problem of multi-source QPAT was considered. The absorption and scattering distributions were estimated using the total variation regularized least-squares method which was solved using the Gauss–Newton algorithm. Both the RTE and the DA were used as forward models for light propagation. The FEM was used for numerical implementations. The approach was investigated in two size domains: in a transport regime and in a diffusive regime.

The simulations show that scaling of the data, for example by using logarithmic data, can be expected to significantly to improve the convergence of the minimization algorithm. Furthermore, in a transport regime, the reconstruction of scattering using the DA is a more ill-posed problem than using the RTE. In a diffusive regime, both models can be expected to be equally reliable. The reconstructions show that both the RTE and the DA can give good estimates for absorption both in a transport regime and in a diffusive regime. However, if the DA is used as a light transport model in a small domain, the estimates for the scattering are significantly worse than when the RTE is used.

Thus, both the RTE and the DA can be used as a forward model in multi-source QPAT. However, depending on the optical properties and the size of the domain, care is needed in the choice of the forward model and in scaling of the data in order to estimate both absorption and scattering accurately.

Acknowledgments

The authors would like to thank Ville Kolehmainen and Teedah Saratoon for useful discussions. This work has been supported by the Academy of Finland (projects 136220, 140984, and 250215 Finnish Centre of Excellence in Inverse Problems Research), by the strategic funding of the University of Eastern Finland, and by the Engineering and Physical Sciences Research Council, UK, EP-SRC (EP/E034950/1 and EP/E050980/1).

References

- [1] Arridge S R 1999 Optical tomography in medical imaging *Inverse Problems* **15** R41–93
- [2] Arridge S R, Kaipio J P, Kolehmainen V, Schweiger M, Somersalo E, Tarvainen T and Vauhkonen M 2006 Approximation errors and model reduction with an application in optical diffusion tomography *Inverse Problems* **22** 175–95
- [3] Bal G and Ren K 2011 Multi-source quantitative photoacoustic tomography in a diffusive regime *Inverse Problems* **27** 075003
- [4] Bal G and Ren K 2012 On multi-spectral quantitative photoacoustic tomography in diffusive regime *Inverse Problems* **28** 025010
- [5] Banerjee B, Bagchi S, Vasu R M and Roy D 2008 Quantitative photoacoustic tomography from boundary pressure measurements: noniterative recovery of optical absorption coefficient from the reconstructed absorbed energy map *J. Opt. Soc. Am. A* **25** 2347–56
- [6] Beard P 2011 Biomedical photoacoustic imaging *Interface Focus* **1** 602–31
- [7] Cox B, Tarvainen T and Arridge S 2011 Multiple illumination quantitative photoacoustic tomography using transport and diffusion models *Tomography and Inverse Transport Theory (Contemporary Mathematics*

- vol 559) ed G Bal, D Finch, P Kuchment, J Schotland, P Stefanov and G Uhlmann (Providence, RI: Americal Mathematical Society) pp 1–12
- [8] Cox B T, Arridge S R, Köstli K P and Beard P C 2006 Two-dimensional quantitative photoacoustic image reconstruction of absorption distributions in scattering media by use of a simple iterative method *Appl. Opt.* **45** 1866–75
- [9] Cox B T, Arridge S R and Beard P C 2009 Estimating chromophore distributions from multiwavelength photoacoustic images *J. Opt. Soc. Am. A* **26** 443–55
- [10] Firbank M, Arridge S R, Schweiger M and Delpy D T 1996 An investigation of light transport through scattering bodies with non-scattering regions *Phys. Med. Biol.* **41** 767–83
- [11] Gao H, Zhao H and Osher S 2010 Bergman methods in quantitative photoacoustic tomography *UCLA CAM Report* 10-24
- [12] Henyey L G and Greenstein J L 1941 Diffuse radiation in the galaxy *AstroPhys. J.* **93** 70–83
- [13] Hristova Y, Kuchment P and Nguyen L 2008 Reconstruction and time reversal in thermoacoustic tomography in acoustically homogeneous and inhomogeneous media *Inverse Problems* **24** 055006
- [14] Ishimaru A 1978 *Wave Propagation and Scattering in Random Media* vol 1 (New York: Academic Press)
- [15] Jetzfellner T, Razansky D, Rosenthal A, Schulz R and Englmeier K-H 2009 Performance of iterative optoacoustic tomography with experimental data *Appl. Phys. Lett.* **95** 013703
- [16] Kaipio J and Somersalo E 2005 *Statistical and Computational Inverse Problems* (New York: Springer)
- [17] Kanschat G 1998 A robust finite element discretization for radiative transfer problems with scattering *East-West J. Numer. Math.* **6** 265–72
- [18] Kolehmainen V, Vauhkonen M, Kaipio J P and Arridge S R 2000 Recovery of piecewise constant coefficients in optical diffusion tomography *Opt. Express* **7** 468–80
- [19] Kowar R and Scherzer O 2010 Photoacoustic imaging taking into account attenuation arXiv:1009.4350
- [20] Kuchment P and Kunyansky L 2008 Mathematics of thermoacoustic tomography *Eur. J. Appl. Math.* **19** 191–224
- [21] Laufer J, Cox B, Zhang E and Beard P 2010 Quantitative determination of chromophore concentrations from 2D photoacoustic images using a nonlinear model-based inversion scheme *Appl. Opt.* **49** 1219–33
- [22] Okada E, Firbank M, Schweiger M, Arridge S R, Cope M and Delpy D T 1997 Theoretical and experimental investigation of near-infrared light propagation in a model of the adult head *Appl. Opt.* **36** 21–31
- [23] Ripoll J and Ntziachristos V 2005 Quantitative point source photoacoustic inversion formulas for scattering and absorbing media *Phys. Rev. E* **71** 031912
- [24] Rosenthal A, Razansky D and Ntziachristos V 2009 Quantitative optoacoustic signal extraction using sparse signal representation *IEEE Trans. Med. Imaging* **28** 1997–2006
- [25] Schweiger M and Arridge S R 1999 Application of temporal filters to time resolved data in optical tomography *Phys. Med. Biol.* **44** 1699–717
- [26] Schweiger M, Arridge S R and Nissilä I 2005 Gauss–Newton method for image reconstruction in diffuse optical tomography *Phys. Med. Biol.* **50** 2365–86
- [27] Shao P, Cox B and Zemp R J 2011 Estimating optical absorption, scattering and Grueneisen distributions with multiple-illumination photoacoustic tomography *Appl. Opt.* **50** 3145–54
- [28] Tarvainen T, Vauhkonen M and Arridge S R 2008 Gauss–Newton reconstruction method for optical tomography using the finite element solution of the radiative transfer equation *J. Quant. Spectrosc. Radiat. Transfer* **109** 2767–78
- [29] Tarvainen T, Vauhkonen M, Kolehmainen V and Kaipio J P 2005 Hybrid radiative transfer–diffusion model for optical tomography *Appl. Opt.* **44** 876–86
- [30] Tervo J, Kolmonen P, Vauhkonen M, Heikkinen L M and Kaipio J P 1999 A finite-element model of electron transport in radiation therapy and a related inverse problem *Inverse Problems* **15** 1345–61
- [31] Treeby B E, Zhang E Z and Cox B T 2010 Photoacoustic tomography in absorbing acoustic media using time reversal *Inverse Problems* **26** 115003
- [32] Wang L and Jacques S L 1993 Hybrid model of Monte Carlo simulation and diffusion theory for light reflectance by turbid media *J. Opt. Soc. Am. A* **10** 1746–52
- [33] Wang L V (ed) 2009 *Photoacoustic Imaging and Spectroscopy* (Boca Raton, FL: CRC Press)
- [34] Xu M and Wang L V 2006 Photoacoustic imaging in biomedicine *Rev. Sci. Instrum.* **77** 041101
- [35] Yao L, Sun Y and Jiang H 2009 Quantitative photoacoustic tomography based on the radiative transfer equation *Opt. Lett.* **34** 1765–7
- [36] Yao L, Sun Y and Jiang H 2010 Transport-based quantitative photoacoustic tomography: simulations and experiments *Phys. Med. Biol.* **55** 1917–34
- [37] Zemp R J 2010 Quantitative photoacoustic tomography with multiple optical sources *Appl. Opt.* **49** 3566–72